International Journal of Impact Engineering 185 (2024) 104843

Contents lists available at ScienceDirect

International Journal of Impact Engineering

journal homepage: www.elsevier.com/locate/ijimpeng

Mechanical response of 6061-T6 aluminium alloy subjected to dynamic testing at low temperature: Experiment and modelling

Mateusz Kopec [a,b,*], Xiaochuan Liu [c], Dominika Gorniewicz [d], Patryk Modrzejewski [d], Dariusz Zasada [d], Stanisław Jóźwiak [d], Jacek Janiszewski [d], Zbigniew L. Kowalewski [a]

[a] Institute of Fundamental Technological Research Polish Academy of Sciences, 5b Pawińskiego Str., 02-106 Warsaw, Poland
[b] Department of Mechanical Engineering, Imperial College London, London SW7 2AZ, UK
[c] School of Mechanical Engineering, Xi'an Jiaotong University, Xi'an, 710049, China
[d] Military University of Technology, 00-908 Warsaw, Poland

ARTICLE INFO

Keywords:
Split Hopkinson pressure bar (SHPB)
Low temperature
AA6061-T6
Microstructure

ABSTRACT

The aim of this research was to investigate an effect of low temperature on the mechanical properties and microstructure of 6061-T6 aluminium alloy (AA6061-T6) subjected to dynamic loading. The specimens were subjected to dynamic compression at a low temperature of −80 °C in a range of strain rates from 1.25×10^3 1/s to 3.4×10^3 1/s to compare their mechanical responses. The deformation mechanisms were analysed through EBSD observations during which dynamic recovery, was found as the dominant one. Furthermore, microstructural analysis indicated that deformation under high strain rate conditions and temperature of -80 °C enables to keep the constant initial grain size of the material after the loading applied. The material behaviour was modelled using mechanism-based viscoplastic constitutive equations. Furthermore, an accuracy of the developed model was validated by comparing it to experimental data. The set of constitutive equations proposed has been successful in modelling the stress-strain behaviour of the material for the range of strain rates and temperatures encountered in aluminium-forming processes under low-temperature conditions.

1. Introduction

An increasing trend for the vehicle weight reduction to lower the greenhouse gas emissions is still the focus of automotive industry. Aluminium alloys of 6xxx series have been widely used in such industry, because of their high machinability, weldability, high strength-weight ratio, good erosion resistance, and relatively low cost [1], making them dominant in vehicle structures over the next 20 years [2]. However, a low formability and large spring back at room temperature limit AA6061 significantly to be formed into complex-shaped components by using conventional forming technologies [3]. AA6061 is also used in construction and favoured over AA6082 due to its lower cost. The novel cryogenic forming processes are able to fundamentally improve the plasticity of aluminium alloys [4], and meanwhile, avoid severe localized thinning [5] and microstructure deterioration [6] that is caused by hot forming. It was found, that the yield strength, ultimate tensile strength and elongation of AA6060 increased by approximately 12 %, 33 % and 48 %, respectively, when the forming temperature decreased from room temperature to −196 °C [7]. Moreover, the formability of AA6061 at −196 °C was even twice of that at room temperature, as stated by Wang et al. [8]. A similar effect of low temperature on the deformation behaviour of 7xxx series aluminium alloys was also observed in the study of Liu et al. [9]. Such behaviour was associated with the dynamic recovery, which was suppressed at low temperature, and thus, the dislocation density and proportion of screw dislocations were increased, leading to the enhanced strain hardening rate, and consequently, material strengthening [10]. In addition, the dislocation was found to be more homogenous at low temperature, resulting in the reduction of slip lines and misorientation, which worked as another deformation mechanism of aluminium alloys under such forming conditions [11]. In other studies, Park et al. [12] investigated the cryogenic mechanical behaviour of 5xxx and 6xxx series aluminium alloys as a function of low temperature (110–293 K) and quasi-static strain rate (10^{-4} and 10^{-2} s^{-1}). It was found, that the strength and ductility of the materials in question improved with a decrease of the temperature, however, a strain rate effect was observed in terms of the ductility for 5xxx series, only. The experimental work performed by Sotirov et al. [13] confirmed the feasibility of low-temperature forming of aluminium

* Corresponding author.
E-mail address: mkopec@ippt.pan.pl (M. Kopec).

https://doi.org/10.1016/j.ijimpeng.2023.104843
Received 24 July 2023; Received in revised form 24 October 2023; Accepted 28 November 2023
Available online 29 November 2023

panels, since the significant improvement of the mechanical response of AA5182 alloy was observed, that was expressed by an enhancement of flow stress, elongation and forming limits. One should highlight, that aluminium alloys have been widely tested at cryogenic conditions, however, most of these studies cover solely the static deformation range. Since the application of higher deformation rates could potentially improve an efficiency of the forming processes, a deformation at high strain rates should be investigated [14].

The adaptation of low-temperature among conventional forming methods including incremental forming [15], deep drawing [16] or hydro-bulging [17] significantly extends the forming window for aluminium alloys. In order to successfully form such materials, the constitutive models have been generally used to predict their deformation behaviour for different forming processes. Lin et al. [18] and Odenberger et al. [19] predicted the flow curves of aluminium alloys and titanium alloys, respectively, at elevated temperatures by using the unified constitutive equations. A hyperelastic-based constitutive model considering the dissipative phenomena of strain-induced phase transformation was developed by Homayounfard et al. [20] to predict the flow curves of stainless steels at low temperature. However, the constitutive model has not been developed as yet, particularly for aluminium alloys under low temperature forming conditions.

Therefore, this paper covers two important aspects: high strain rate deformation of the AA6061-T6 under low-temperature conditions and subsequent modelling of its stress-strain response by using the visco-plastic approach. The mechanical behaviour was investigated through the tests on Split Hopkinson Pressure Bar (SHPB) and the microstructural evolution monitored by using Scanning Electron Microscopy (SEM) and Electron Backscatter Diffraction (EBSD). The response of aluminium alloy deformed at low temperature was further compared to its room temperature behaviour in order to identify the deformation mechanisms.

2. Materials and methods

2.1. Microstructural characteristics of the as-received AA6061-T6

The microstructure of the as-received, commercial AA6061-T6 tested in this research was presented in Fig. 1 in the form of an Inverse Pole Figure (IPF) and Kernel Average Misorientation (KAM) maps. The T6 temper designation means that the AA6061 has been subjected to a solution heat treatment followed by quenching, cooling, and aging. Artificially aging enables the material to achieve the desired precipitation hardening. This alloys has a face centred cubic crystal structure (FCC), with 12 slip systems and has a high stacking fault energy compared to most metals. The undeformed material exhibits equiaxed grains of an average size equal to 50 ± 20 μm without preferred grain orientation (Fig. 2a). The high fraction of low misorientation observed in Fig. 1b may suggest the low dislocation density of the as-received material.

2.2. Mechanical testing

Dynamic testing was carried out by using the SHPB setup with low-temperature environmental chamber. It is the most used technique for material testing at high strain rates [21]. Typical SHPB consists of a striker bar, input, and output bars, between which a cylindrical specimen is placed, Fig. 2. All bars of the SHPB device are made of the maraging steel (heat-treated MS350 grade: yield strength – 2300 MPa; elastic wave speed – 4960 m/s) with diameter of 12 mm. The lengths of the striker bar and input bar, as well as the output bar, were 250 and 1200 mm, respectively. The striker bar is driven by a gas gun with a barrel length of 1200 mm and inner diameter of 12.1 mm. To minimize the wave dispersion and to facilitate stress equilibrium, the pulse shapers were used [22]. They had a shape of a disc made of copper and were placed on the impact end of the input bar. Trial tests were conducted to find the appropriate size of the pulse shaper. It was found, that for a given SHPB test condition (i.e., mainly at striker bar impact), the copper pulse shaper with the diameter of 3 mm and thickness of 0.1, 0.2 or 0.3 mm ensures damping of the high-frequency oscillations.

Dynamic compression curves were plotted using the well-known formulas according to the classical Kolsky theory [23,24] based on the single-wave analysis method, which assumes stress equilibrium for specimen under given testing conditions. The strain and strain rate in the specimens were calculated applying the reflected wave profile (ε_r), whereas the plastic flow stress in the specimen was determined from

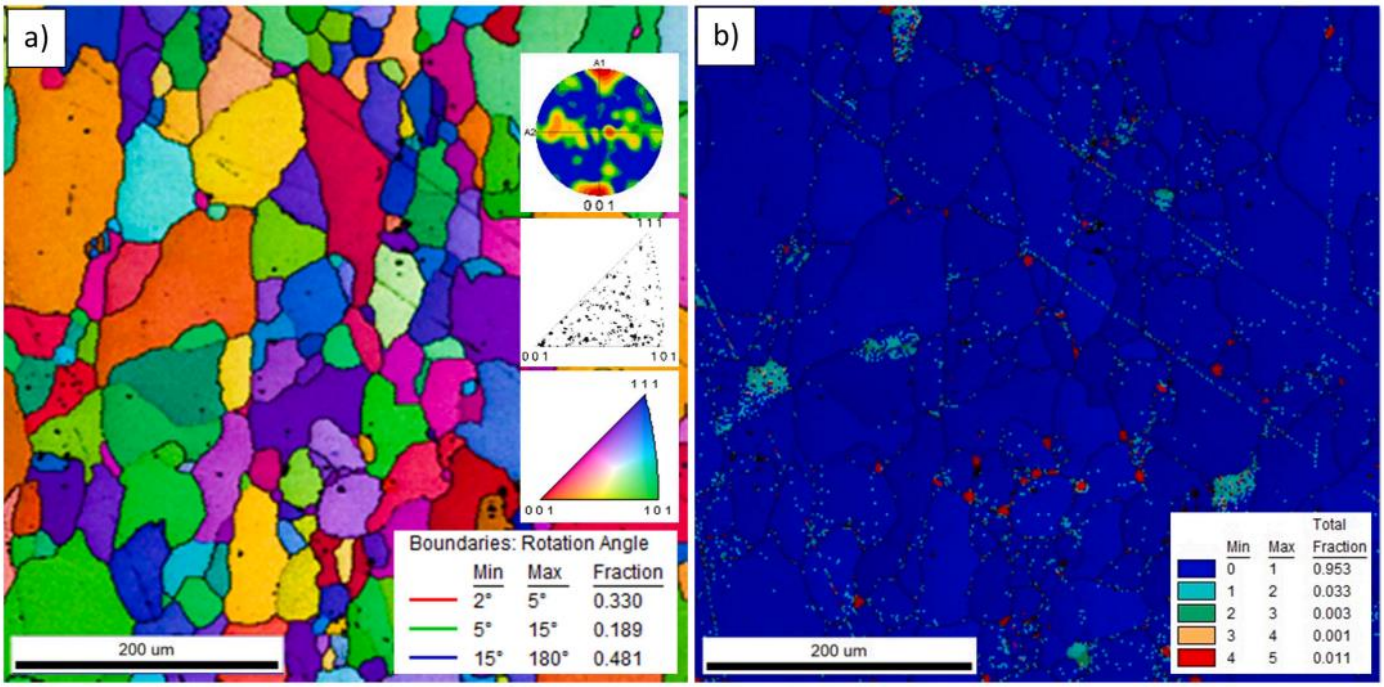

Fig. 1. IPF (a) and KAM (b) map of the as-received AA6061-T6.

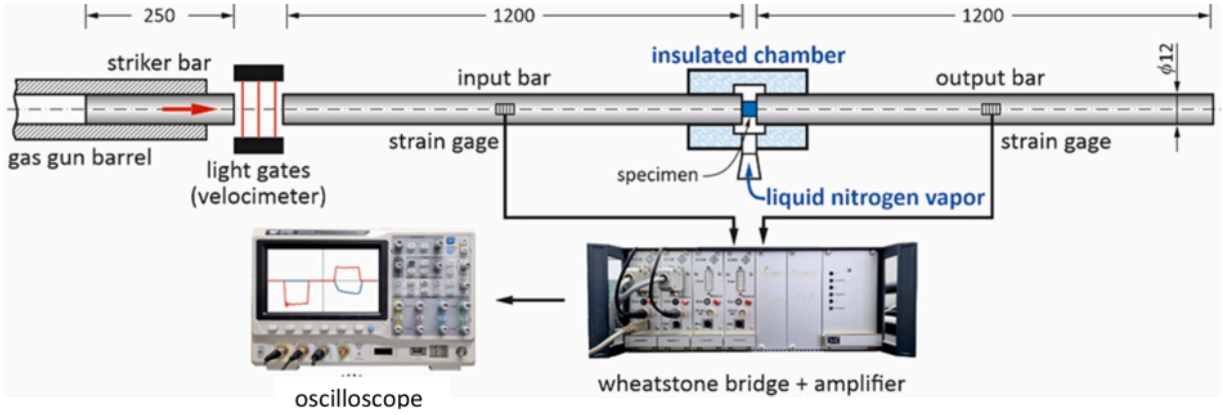

Fig. 2. Scheme of the SHPB system equipped with the environmental chamber for low-temperature testing.

transmitted wave profile (ε_t). Wave signals were measured by pairs of strain gages (gage length – 1.5 mm; resistance - 350 Ohm) located at the half-length of the input and output bars (Fig. 2). The signals from the strain gages were conditioned by the data-acquisition system including a Wheatstone bridge, signal amplifier of the cut-off frequency equal to 1 MHz and digital oscilloscope.

The dynamic tests at low temperature were conducted in the insulated chamber inside which the specimens machined from the extruded bar to cylindric specimens of 5 mm × 5 mm were cooled down using liquid nitrogen. The chamber made of high-density polystyrene foam was divided into two parts, upper and lower, to facilitate its assembly on the Hopkinson bars and the placement of specimen between the bars. The chamber was equipped with a window through which the liquid nitrogen was flushed. A thermocouple feedback processing controller was used to control the flow liquid nitrogen using the cryogenic electrovalve. The thermocouple was in contact with the specimen from its upper side, i.e. on the side opposite to the specimen surface, which was cooled with liquid nitrogen vapour. In this way, the amount of liquid nitrogen flushed into the chamber was controlled to keep a constant temperature for a long time. Based on the preliminary tests with reference specimen (specimen with a small hole in which the thermocouple was placed in the centre of the longitudinal specimen axis), it was found out that after reaching the desired level, the temperature was held constant for at least 5 min to ensure no temperature gradient throughout the specimen. The mechanical properties of the aluminium alloy were characterized at strain rates ranging from 1.25×10^3 1/s to 3.40×10^3 1/s and a temperature of −80 °C. The additional tests under the same conditions, however, at room temperature were performed for the comparative studies. All the stress data were provided in nominal stress (force/original cross-sectional area of the material before any deformation).

2.3. Microstructural observations

The microstructure of deformed specimens was characterized by SEM. Prior to the study, the specimens were firstly cold-mounted, and then, polished using Struers MD-Largo disc dedicated to soft materials of 40–150HV and 9 μm diamond suspension. The polishing was performed using Metrep® MD-Chem cloth and 0.04 μm Colloidal Silica solution. The microstructural characterization was performed on high-resolution Quanta 3D FEG (SEM/FIB) scanning electron microscope system equipped with an integrated EDS/EBSD system (EDS - energy dispersive X-ray detector, and EBSD - electron backscatter diffraction analysis system) operated at 20 kV. The average grain size was calculated by using NIS Elements software on the image magnification of 500x.

3. Results and discussion

3.1. Determination of AA6061-T6 flow stress under dynamic testing and low-temperature conditions

Fig. 3 presents the stress-strain curves of AA6061-T6 determined from dynamic tests at room temperature and −80 °C. The alloy in question exhibited a rise of the plastic flow stress and maximum stress at the low-temperature. Each value was obtained by measuring at least two specimens and experiments showed a standard deviation less than 5 %. In comparison to the room temperature testing, a relative improvement in nominal stress of approximately 10 % was achieved regardless of the strain rate used. On the other hand, a much lower increase of the plastic flow stress was observed (around 5 %). The higher increase in the nominal stress compared to that of the plastic flow stress was related to the faster strengthening of the material at low temperature.

In addition, based on the mechanical response of aluminium alloy subjected to dynamic compression, one can observe, that dynamic curves have a slightly different slope. It suggests, that depending on the strain rate applied, the hardening phenomenon of different intensity occurred. The hardening effect was assessed in this research through the analysis of the linear, plastic-flow part of each stress-strain curve, Fig. 4. For each part, the linear function was applied to fit experimental data. A value of slope coefficient of the linear function serves as a hardening indicator. It was found, that for tests carried out under a lower strain rate, the hardening rate is higher. This is in contradiction with the relations determined during standard static testing. Such behaviour is directly related to the adiabatic heating of specimen during dynamic testing. The effect of thermal softening due to adiabatic heating under high strain rate loading was reported by Ma et al. [25] and Soares et al. [26]. It was also observed under low-temperature testing conditions [27]. The specimens temperature subjected to the high-strain rate impact is rising due to the conversion of the mechanical energy into the heat. The slope variation representing hardening evolution can be also explained by dynamic recovery changes since its inhibited dynamics under low-temperature conditions leads to higher dislocation density, and therefore, higher strain hardening rates [28].

3.2. Coupled effects of low temperature and high strain rate on AA6061-T6 alloy microstructure evolution

The microstructural evolution observations were performed by using SEM-EBSD investigations and presented in the form of IPF and KAM maps (Figs. 5 and 6). One should conclude, that dynamic deformation at the strain rate of 1.25×10^3 1/s led to a significant increase of low-angle boundaries (LAB) since their fraction increased from 0.330 in the as-received state to 0.629 and 0.642 at room temperature and −80 °C, respectively (Table 1, Fig. 7). It can be also observed, that dynamic

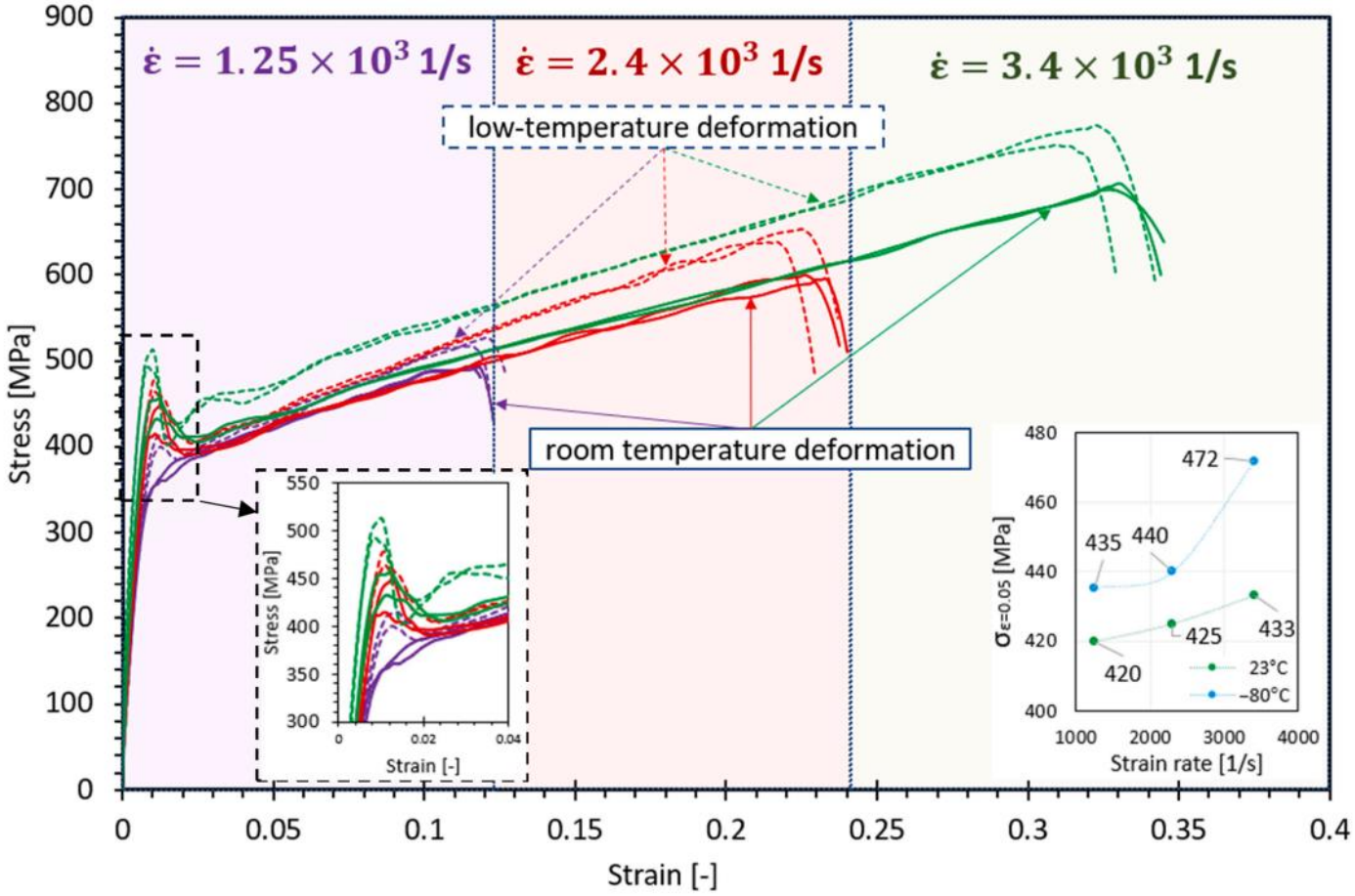

Fig. 3. Comparison of dynamic stress-strain characteristics of AA6061-T6 compressed under different values of strain rate and temperature.

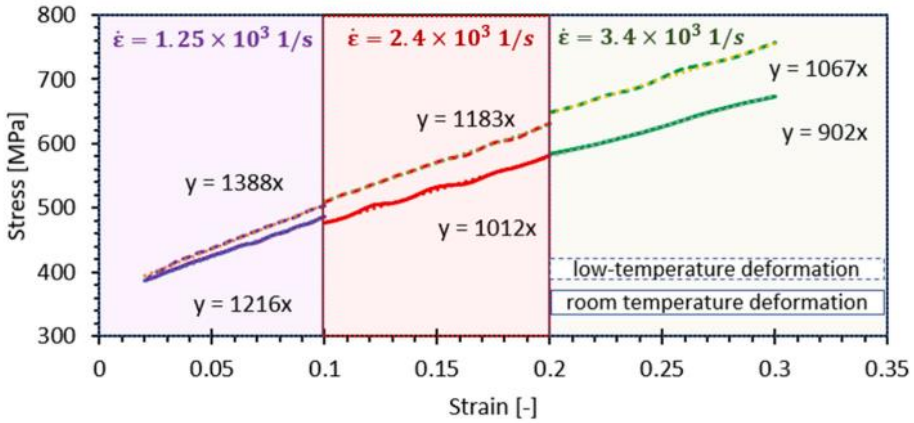

Fig. 4. Comparison of the hardening rate of AA6061-T6 compressed under different values of strain rate and temperature.

testing at room temperature is leading to the prominent orientation in [001] direction (Fig. 5a) while the low-temperature condition keeps the orientation at the state similar to the as-received material (Fig. 5b). On the other hand, significant differences in KAM maps can be observed. The blue colour in these maps represents low values of misorientation while the red - large ones. The average KAM values tend to increase with increasing strain rate and are higher at room temperature. One should indicate, that higher KAM values are observed at grain boundaries, however, after low-temperature deformation, some regions of large grains still exhibit areas with relatively low KAM values. Dynamic compression at the highest strain rate considered in this research (3.4×10^3 1/s) led to a severe deformation of grains with numerous slip bands visible (Figs. 6 and 7). However, after low-temperature testing, the slip lines are clearly less pronounced and the grains accommodate the process of deformation more evenly, providing a fewer areas of KAM < 3. Generally, it could be observed that RT compression leads more likely to slip lines formation, whereas under low-temperature conditions a general reduction of slip lines and a smaller number of highly deformed areas can be observed (Fig. 7). Such effect enabled to conclude, that the same slip systems are activated during deformation at room and low temperature. Similar behaviour was reported by Gruber et al. [28]. The changes in deformed material at the same strain rate but under different

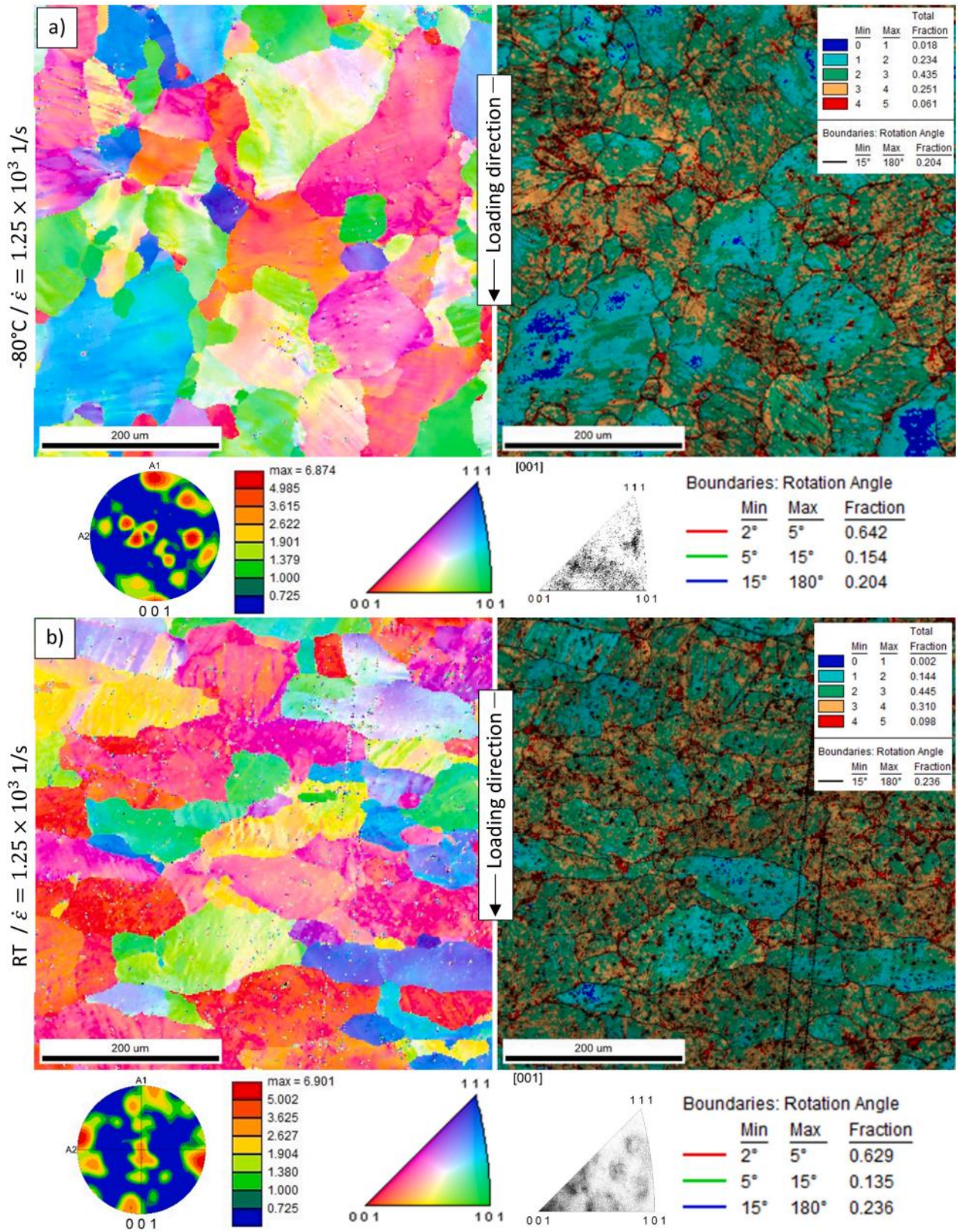

Fig. 5. Comparison of the IPF and KAM maps for AA6061-T6 specimens deformed at the strain rate of 1.25 × 10^3 1/s under low-temperature conditions (a) and at room temperature (b).

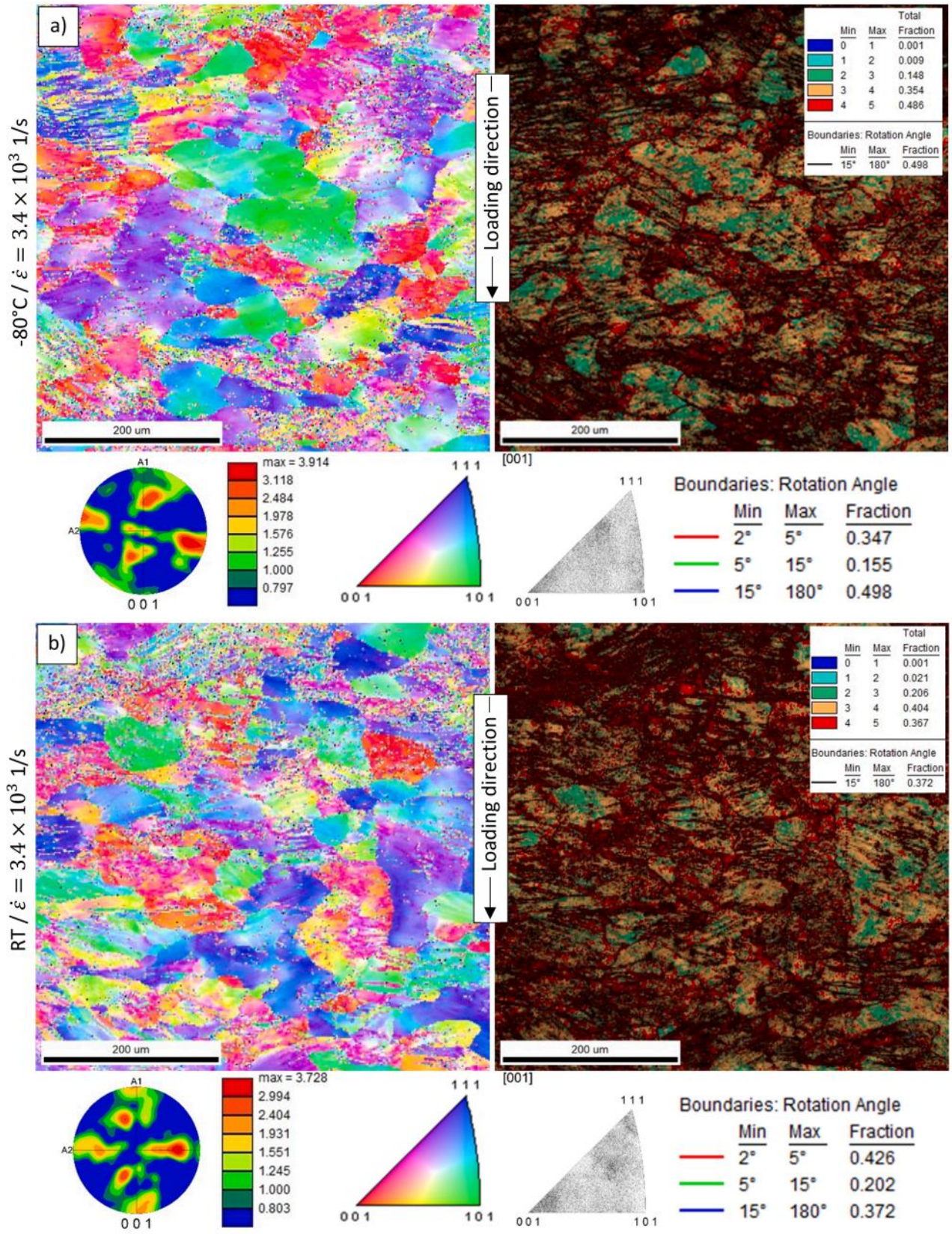

Fig. 6. Comparison of the IPF and KAM maps for AA6061-T6 specimens deformed at the strain rate of 3.4 × 10^3 1/s under low-temperature conditions (a) and at room temperature (b).

Table 1
Misorientation angle values for different strain rates.

	$\dot{\varepsilon} = 1.25 \times 10^3$ 1/s			$\dot{\varepsilon} = 3.4 \times 10^3$ 1/s		
	2°–5°	5°–15°	15°–180°	2°–5°	5°–15°	15°–180°
As-received material	0.330	0.189	0.481	0.330	0.189	0.481
Deformed at room temperature	0.629	0.135	0.236	0.426	0.202	0.372
Deformed at −80 °C	0.642	0.154	0.204	0.347	0.155	0.498

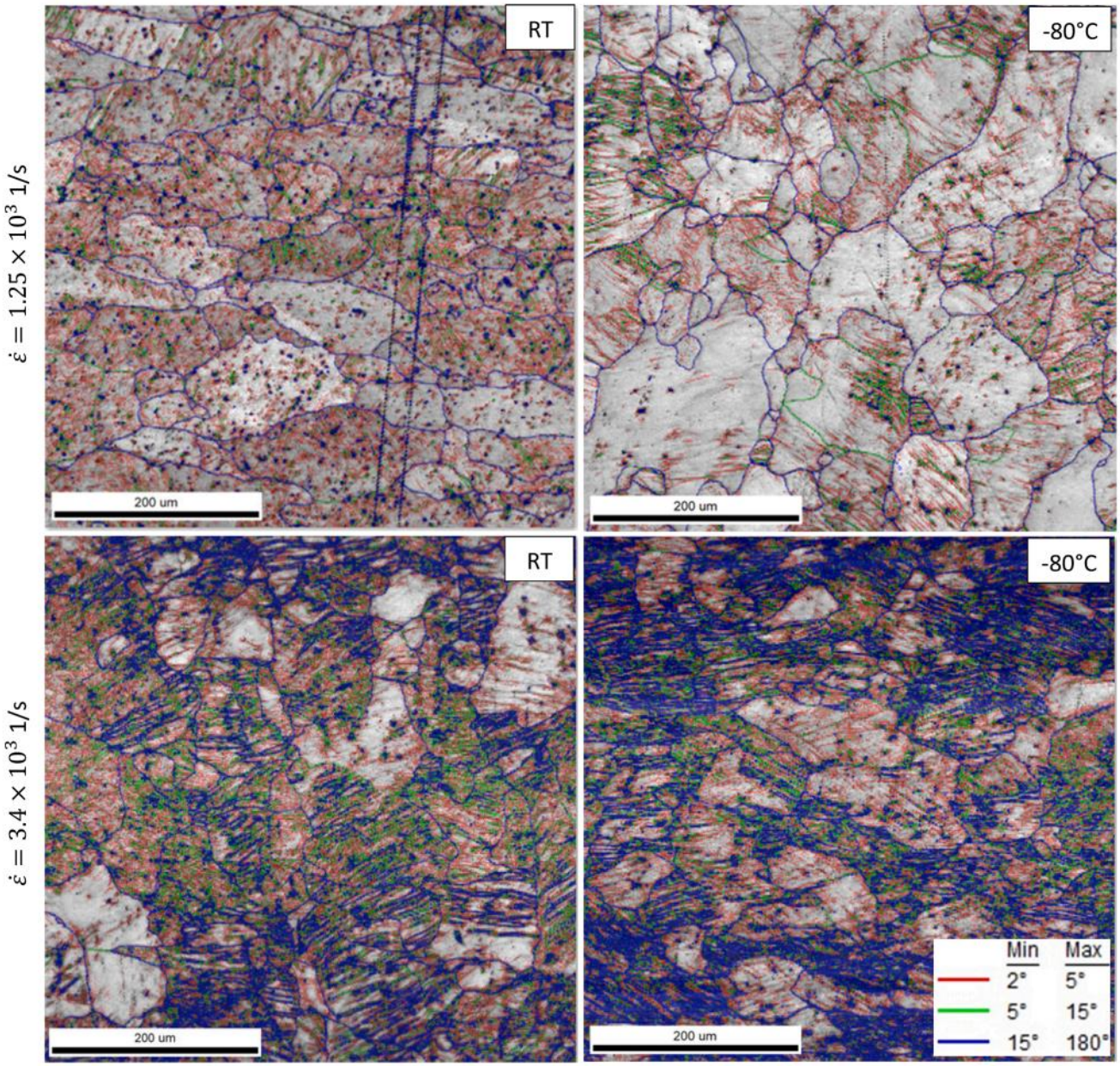

Fig. 7. Grain boundaries after deformation under different temperature and strain rate conditions.

temperature conditions could be explained by analysis of the relative dislocation density ratio. It is known, that material recovery is more dominant at room than at low temperature [28]. Under the same strain rate applied, more dislocation annihilation should occur at room temperature. On the other hand, the hardening of tested material is dominant at low temperature, and as consequence, the recovery appears slower. This is attributed to the fact, that the same number of dislocations is required to reach a certain level of deformation, however, the room temperature under which the deformation occurs accelerates the recovery.

Similar findings were presented by Gruber et al. [28] who explained the hardening-dislocation density dependence. It was concluded, that by lowering the temperature, dislocation generation remains constant while dynamic recovery reduces, leading to a higher dislocation density, and therefore, a higher strain hardening rate. Such phenomenon is responsible for the higher strength of the alloys at low temperatures in comparison to that obtained due to deformation at room temperature.

One could notice, that the number of shear bands is much higher in

smaller grains (Fig. 7). It is related to the fact, that the mean free path of dislocations in smaller grains is much shorter [29], which leads to faster blocking of defects at primary grain boundaries, and subsequently, to the formation of shear bands. The formation of shear bands is a strain rate-dependent phenomenon. It is known, the mechanical energy carried by the stress wave in the experiment of SHPB must be dissipated by the specimen during deformation. When the lower strain rate of 1.25×10^3 1/s is considered, there are no significant changes in misorientation angle values (Table 1) at both, low and room temperature. On the other hand, the deformation under the strain rate of 3.4×10^3 1/s introduces a significant amount of energy, which must be dissipated. The generation of heat during dynamic deformation leads to the intensification of dynamic recovery effects: a decrease in the number of dislocations and the formation of shear bands (Table1, Fig. 7), that cause the more prominent material hardening under low-temperature conditions (Fig. 4) [30]. The process of dynamic recovery in metals that do not undergo dynamic recrystallization causes the formation of perfectly ordered, low-energy dislocation systems (strongly ordered sub-boundaries). Such a phenomenon is related to the annihilation and rearrangement of dislocations [31,32]. An intensive recovery process prevents the concentration of strain energy, which could create favourable conditions for the initiation of dynamic recrystallization. Hardening of the material in the initial deformation period, before reaching the steady-state flow range, is therefore associated with an increase of the dislocation density and the formation of a cellular dislocation and sub-grain structures [33]. In case of investigated AA6061-T6 material, such increase of dislocation density is also associated with activation of different slip systems due to intensification of interactions between the mobile and the stored dislocations in the dislocation forest [34], and/or Mg_2Si precipitations responsible for material hardening [35]. Furthermore, the dislocation climbing rate during plastic deformation increases with increasing deformation. As a result, the frequency of annihilation increases, reaching the value characteristic for the equilibrium state. Therefore, the created dislocation substructure and sub-grains are characterized by a constant disorientation angle, which in static conditions would cause further deformation under constant stress. However, for dynamic processes, the newly formed dislocations are rearranged into new substructures and walls of dislocation cells [36].

The as-received AA6061-T6 was characterized by an average grain size of 50 μm ±20 μm. The dynamic deformation applied by using SHPB under both, room and low temperature did not affect its evolution significantly, since only the grain shape is changing, not their equivalent size (Fig. 8). Although a slight grain sizes increase was found under the strain rate of 1.25×10^3 1/s, their average sizes obtained for the highest strain rate were almost the same as those for the as-received material. Thus, it could be concluded, that in terms of changes in the average grain size, AA6061-T6 is not sensitive to high strain rate deformation under both room and low temperature conditions.

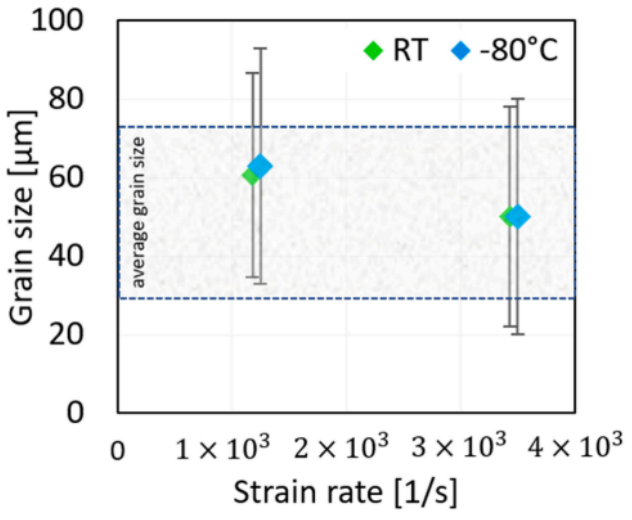

Fig. 8. Comparison of the average grain size distribution as a function of strain rate at room and low temperature.

4. Material modelling and model calibration

The successful modelling of material behaviour requires representative equations reflecting the key mechanisms involved during deformation. For metal stamping processes, the flow stress can be described according to the Hooke's law:

$$\sigma = E(\varepsilon_T - \varepsilon_P) \tag{1}$$

where ε_T- total strain, ε_p - plastic strain, and E - Young's modulus. Taking into account the viscoplastic flow, the rate of plastic deformation can be determined by the instantaneous flow stress, initial yield stress and isotropic dislocation hardening. Hence, it can be expressed by the following equation:

$$\dot{\varepsilon}_P = \left(\frac{\sigma - H - k}{K}\right)^{n_1} \tag{2}$$

where $\dot{\varepsilon}_p$ - plastic strain rate, σ - flow stress, H - stress due to dislocation hardening, k - initial yield stress, and K, n_1 - material constants. Since dynamic deformation under low-temperature conditions did not affect the grain size considerably (Fig. 8), the developed model does not include grain size evolution and softening caused by dynamic recrystallization.

According to the classic work-hardening theory [37–39], the hardening parameter H in Eq. (2) depends on the dislocation density ρ:

$$H = B\overline{\rho}^{0.5} \tag{3}$$

The dislocation density evolution from 0 in the initial state to 1 in the saturated state involves dislocation accumulation due to plastic flow and dynamic recovery, and concurrent dislocation annihilation due to static recovery, which can be calculated as:

$$\dot{\overline{\rho}} = \mathrm{A}(1 - \overline{\rho})\dot{\varepsilon}_P - C\overline{\rho} \tag{4}$$

where $\overline{\rho}$- normalized dislocation density, and A and C are the material parameters.

Under the low-temperature conditions, the yield stress incorporates thermally activated mechanisms in addition to the plastic deformation caused by dislocations and it is directly related to the reduction of undissolved alloying elements, of which the evolutionary process can be described as:

$$\dot{k} = D\dot{\varepsilon}_P^{n_2} \tag{5}$$

where D - temperature-dependent diffusion parameter of alloying elements, n_2 - material constant. It has to be emphasized that K, n_1, n_2, B, A and C depend on the instantaneous temperature, which can be well expressed by using the Arrhenius equation:

$$X = X_0 \exp\left(\frac{Q_X}{RT}\right) \tag{6}$$

where X_0 - coefficient of the applied parameter, R - universal gas constant of 8.314 J/(molK), T - absolute temperature and Q_X - activation energy.

The set of constitutive equations Eqs. (1)–((6)) developed to characterise the flow behaviour of AA6061-T6 under low-temperature conditions, of which the experimental results are shown in Fig. 9 as the symbols. Subsequently the material constants are calibrated and optimised (Table 2) by using Genetic Algorithm, of which the flow chart is shown in Fig. 10, resulting in the predicted solid lines in Fig. 9.

As can be seen, a good agreement between the experimental data

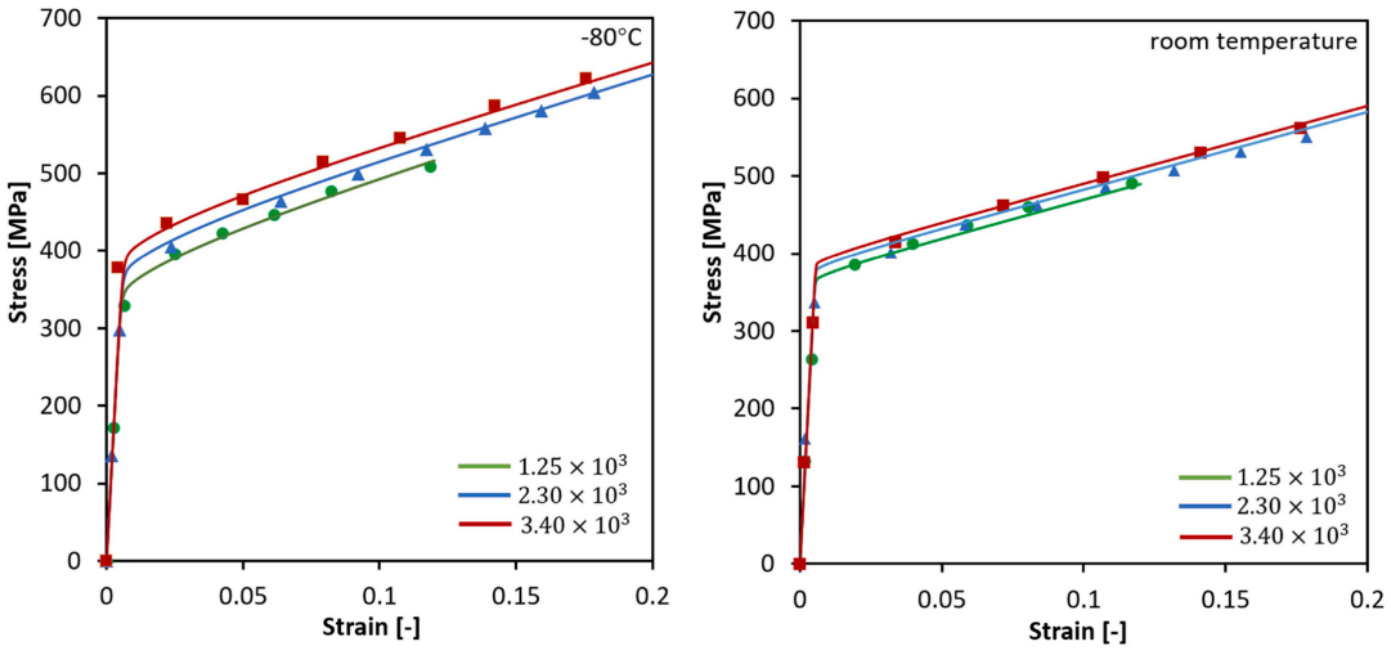

Fig. 9. Comparison of the stress - strain curves obtained from the experiments and numerical calculations at room and low temperature (dot data: experimental results, line data: modelling results).

Table 2
Material parameters of the model.

Constant	E	Q_E	K_0	Q_K	H_0	Q_B
Value	80,419	−339.9	502.1	−3630.6	0.48	7445.3
Unit	MPa	J/mol	MPa	J/mol	MPa	J/mol
Constant	C_0	Q_C	A_0	Q_A	D_0	Q_D
Value	0.272	3192.1	300.8	−4384.9	50.291	140.000
Unit	–	J/mol	–	J/mol	MPa	J/mol
Constant	n_1	Q_{n1}	n_2	Q_{n2}	k_0	Q_k
Value	46.57	−3549	1.1	−237.5	176.3	−563.5
Unit	–	J/mol	–	J/mol	MPa	J/mol

(symbols) and numerical calculations (solid lines) was achieved at the temperature range from room temperature to −80 °C and the strain rate range from 1.25×10^3 1/s to 3.4×10^3 1/s. In addition, the developed model was potentially able to predict the stress-strain curves of AA6061-T6 at the low temperature up to −273 °C and strain rate up to 10^5 1/s, which would be verified in future study. One can find, that the relatively low strain-rate sensitivity of aluminium enables an application of the classical viscoplastic model to simulate its deformation characteristics under low-temperature conditions. Thus, the applied model can be regarded as a suitable tool for determination of the material behaviour within finite element analysis.

5. Conclusions

In this study, the low-temperature mechanical behaviour of AA6061-T6 was investigated using SHPB at different temperature and strain rate conditions. In addition, the EBSD observations were performed to analyse the microstructural data. The main findings are summarized as follows:

- The aluminium alloy exhibited relatively low temperature and strain rate dependency since with the temperature decrease to −80 °C, the typical stress parameters like those describing yielding process initiation and maximum stress increased by around 5–10 %, only.
- Microstructural analysis indicated that deformation under high strain rate conditions and temperature of −80 °C enables to keep the constant initial grain size of the material after the loading applied.
- The alloy was able to absorb more energy at low-temperature while achieving the same deformation level as that obtained during the room temperature test. Such phenomena were related to the higher dislocation density, and as a consequence, higher strain hardening rate responsible for the improved strength of the alloy at low temperatures.
- The main deformation mechanism of aluminium alloy subjected to dynamic deformation under low-temperature conditions was represented by dynamic recovery.
- The constitutive equations proposed for aluminium alloy were developed based on the dominant modes of deformation observed during the high strain rate deformation. However, the response of aluminium alloy is highly sensitive to the deformation path. The set of constitutive equations proposed has been successful in modelling of the stress-strain behaviour of the material for the range of strain rate and temperature values encountered in aluminium alloy-forming processes under low-temperature conditions.

CRediT authorship contribution statement

Mateusz Kopec: Conceptualization, Methodology, Validation, Formal analysis, Investigation, Resources, Writing – original draft, Supervision, Project administration. **Xiaochuan Liu:** Software, Data curation, Resources, Writing – original draft. **Dominika Gorniewicz:** Investigation, Data curation, Visualization. **Patryk Modrzejewski:** Investigation. **Dariusz Zasada:** Investigation. **Stanisław Jóźwiak:** Validation, Formal analysis, Resources. **Jacek Janiszewski:** Methodology, Validation, Investigation, Resources. **Zbigniew L. Kowalewski:** Resources, Writing – review & editing.

Declaration of Competing Interest

The authors declare that they have no known competing financial interests or personal relationships that could have appeared to influence the work reported in this paper.

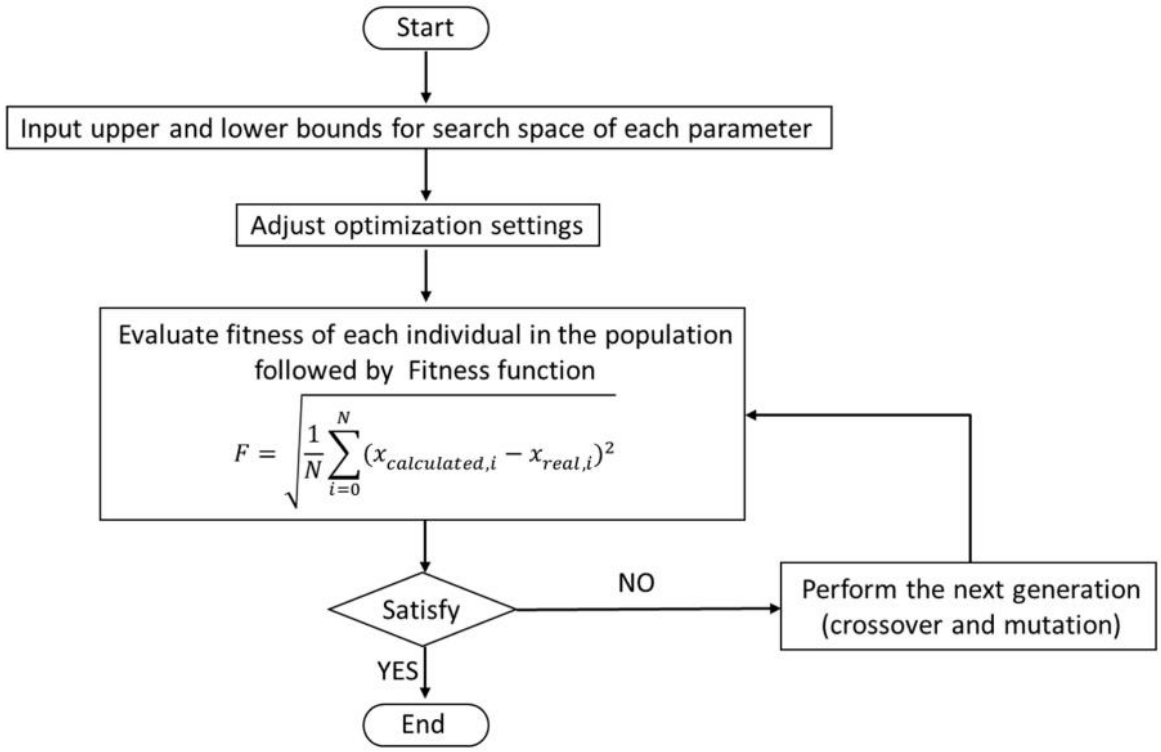

Fig. 10. The flow chart of Genetic Algorithm to calibrate and optimize the viscoplastic constitutive equations.

Data availability

Data will be made available on request.

References

[1] Zhu M, Yang S, Bai Y, Fan C. Mater Res Express 2021;8:056505.
[2] Liu X, Cai Z, Zheng Y, El Fakir O, Gandra J, Wang L. Appl Therm Eng 2020;181:115619.
[3] Zhang X, Huang Y, Wang Y, Shen W, Cui J, Li G, Deng H. J Manuf Process 2022;84:902–12.
[4] Lulay KE, Khan K, Chaaya D. J Mater Eng Perform 2002;11:479–80.
[5] Gao H, El Fakir O, Wang L, Politis DJ, Li Z. Int J Mech Sci 2017;131–132:792–810.
[6] Talebi-Anaraki A, Chougan M, Loh-Mousavi M, Maeno T. J Manuf Mater Process 2020;4:56.
[7] Xu Z, Roven HJ, Jia Z. Mater Sci Eng A 2015;648:350–8.
[8] Wang X, Fan X, Chen X, Yuan S. J Mater Process Technol 2022;306:117649.
[9] Liu W, Hao Y. Mech Mater 2021;163:104080.
[10] Park DY, Niewczas M. Mater Sci Eng A 2008;491:88–102.
[11] Gruber B, Grabner F, Falkinger G, Schökel A, Spieckermann F, Uggowitzer PJ, Pogatscher S. Mater Des 2020;193:108819.
[12] Park D-H, Choi S-W, Kim J-H, Lee J-M. Cryogenics 2015;68:44–58.
[13] Sotirov N, Falkinger G, Grabner F, Schmid G, Schneider R, Grant RJ, Kelsch R, Radlmayr K, Scheerer M, Reichl C, Sehrschön H, Loipetsberger M. Mater Today: Proc 2015;2:S113–8.
[14] Wang K, Kopec M, Chang S, Qu B, Liu J, Politis DJ, Wang L, Liu G. Mater Des 2020;194:108948.
[15] Vanhove H, Mohammadi A, Duflou JR. AIP Conf Proc 2016;1769:070020.
[16] M.Tulke AWolf, Brosius A. IOP Conf Ser 2021;1157:012053.
[17] Wang X, Fan X, Chen X, Yuan S. J Mater Process Technol 2022;303:117532.
[18] Lin J, Liu Y. J Mater Process Technol 2003;143–144:281–5.
[19] Odenberger EL, Schill M, Oldenburg M. Int J Mater Form 2013;6:403–16.
[20] Homayounfard M, Ganjiani M. Int J Plast 2022;156:103344.
[21] Chenand W, Song B. B: *split Hopkinson (Kolsky) Bar*. New York, NY: Springer; 2011.
[22] Panowicz R, Janiszewski J, Kochanowski K. J Theor Appl Mech 2018;56:1217–21.
[23] Kolsky H. Appl Mech Rev 1958;11:465–8.
[24] Kolsky H. J Sound Vib 1964;1:88–110.
[25] Ma SG, Jiao ZM, Qiao JW, Yang HJ, Zhang Y, Wang ZH. Mater Sci Eng A 2016;649:35–8.
[26] Soares GC, Patnamsetty M, Peura P, Hokka M. J. Dyn. Behav. Mater. 2019;5:320–30.
[27] Kim M-S, Lee T, Son Y, Park J, Kim M, Eun H, Park J-W, Kim Y. Processes 2022;10:2401.
[28] Gruber B, Weißensteiner I, Kremmer T, Grabner F, Falkinger G, Schökel Al, Spieckermann Fl, Schäublin R, Uggowitzer PJ, Pogatscher S. Mater Sci Eng A 2020;795:139935.
[29] Adachi H, Mizowaki H, Hirata M, Okai D, Nakanishi H. Mater Trans 2021;62:62–8.
[30] Su L, Deng G, Luzin V, Wang H, Wang Z, Yu H, Li H, Tieu AK. Mater Sci Eng A 2020;780:139190.
[31] Sakai T, Belyakov A, Kaibyshev R, Miura H, Jonas JJ. Prog Mater Sci 2014;60:130–207.
[32] Kopec M, Gorniewicz D, Jóźwiak S, Janiszewski J, Kowalewski ZL. MRS Commun 2023;13:1–8.
[33] Sedláček R, Blum W, Kratochvíl J, Forest S. Metall Mater Trans A 2002;33:319–27.
[34] Bahrami A, Miroux A, Sietsma J. Metall Mater Trans A 2013;44:2409–17.
[35] Moharami A, Razaghian A, Babaei B, Ojo O, Šlapáková M. J Compos Mater 2020;54(26):4035–57.
[36] Hing C, Huang X, Winther G. Philos Mag 2013;93(23):3118–41.
[37] Garrett RP, Lin J, Dean TA. Int J Plast 2005;21:1640–57.
[38] Schneider R, Grant RJ, Sotirov N, Falkinger G, Grabner F, Reichl C, Scheerer M, Heine B, Zouaoui Z. Mater Des 2015;88:659–66.
[39] Lee W-S, Lin C-R. Cryogenics 2016;79:26–34.